High-quantum efficiency of Au@LiNbO₃ core–shell nano composite as a photodetector by two-step laser ablation in liquid

Marwa S. Alwazny[1] · Raid A. Ismail[1] · Evan T. Salim[1]

Abstract

Hybrid and novel Gold core Lithium niobate shell (Au@LiNbO₃, Au@LN) nanoparticles were prepared for the first time by two steps of laser ablation in liquid at different laser fluences. X-ray diffraction, Raman scattering, UV–Visible spectrophotometer, and transmission electron microscope were used to investigate the structural and optical properties of the core–shell nanoparticles. The X-ray diffraction results show that the synthesized Au@LiNbO₃ core–shell nanoparticles are polycrystalline in nature, with 2 J/cm² being the highest crystallinity nanoparticles. Transmission electron microscope studies show the formation of core–shell morphology and the size of the core and shell thickness depends on the laser fluence. The optical absorption of nanocomposites showed the presence of a plasmon peak related to gold (Au) at 500 nm. The energy gap of Au@LiNbO₃ increased from 3.5 to 3.8 eV as laser fluence increased. The presence of active phonons was revealed by Raman results. The current–voltage characteristics of Au@LiNbO₃/Silicon (Si) heterojunction in the dark and illumination are studied as a function of laser fluence. The maximum responsivity and detectivity are 0.69 A/W and 6.5×10^{12} Jones at 380 nm, respectively, for Au@LiNbO₃/p-Si isotype heterojunction photodetector fabricated at 1.3 J/cm² laser fluence. The Energy band diagram of Au@LiNbO₃ core–shell nanoparticles under illumination is constructed.

Keywords Au@LiNbO₃ · Core shell · Laser ablation · Surface plasmon resonance · Photodetector

1 Introduction

Recently, the core/shell nanocomposite nanostructures have drawn attention due to their excellent properties, including mono dispersion, high functionality, stability, reactivity, and self-assembly [1–3]. Furthermore, the noble metal nanoparticles used for the core–shell structure were very attractive and promising composite nanostructures because of the strong coupling exciton between the surface plasmon resonance (SPR) of the noble metal and the semiconductor exciton [4, 5]. In addition to semiconductors, alkaline niobates like lithium, potassium, and sodium niobate (Li-, K-, and NaNbO₃) offer an alternative material for local light delivery via spectral filtering from nonlinear optical effects [6]. Due to its excellent physicochemical, ferroelectric, piezoelectric,

and nonlinear optical properties [7], lithium niobate (LN) has been used in many potential applications, such as electro-optic devices, surface acoustic wave devices, memory units, and neuromorphic systems [8, 9]. Many routes were employed to prepare LiNbO₃ nanoparticles, solution phase, citrate gel, electro spinning, and sol–gel [10–12]. Several attempts to synthesize niobate with gold and silver have been reported. For example, Ghosh et al. [13] prepared nanoshells of lithium niobate with thicknesses ranging from 2.2 to 22 nm around silver as a core in a silicate glass matrix. Niobate is placed in a molten bath of silver nitrate at 588 K for 2 h to experience a lithium⁺ ↔ silver⁺ (Li⁺ ↔ Ag⁺) ion exchange reaction. Few papers were reported on the preparation of LiNbO₃/Si heterojunctions, Hao et al. study the buffer zinc oxide (ZnO) film on the properties of LiNbO₃/n-Si heterojunction photodetector prepared by pulsed laser deposition [14]. Li et al. demonstrated the fabrication of iron doped (Fe-doped) LiNbO₃/n-Si heterojunction that can be used for electro-photonics and integrated optics [15]. Richter et al. [7] synthesized core–shell nanowires from potassium niobate (KNbO₃) cores and a gold shell. They identify two distinct functionalization schemes of core material prior to

✉ Evan T. Salim
  evan_tarq@yahoo.com; evan.t.salim@uotechnology.edu.iq

  Raid A. Ismail
  raidismail@yahoo.com

[1] Applied Science Department, University of Technology-Iraq, Baghdad, Iraq

the shell growth process: silanization and polyelectrolyte. To improve the properties and explore novel routes used for the first time to synthesis of Au@LiNbO$_3$ core–shell, it has demonstrated the colloidal synthesize of the Au@ LiNbO$_3$ core–shell nanoparticles by laser ablation in a liquid environment. The effects of laser fluence on the optical and structural properties of the Au@LiNbO$_3$ core–shell structure were investigated. Furthermore, the optoelectronic properties of the hybrid Au@LiNbO$_3$/Si photodetector were studied and discussed. Preparation of the core–shell structure using the laser ablation in liquid (LAL) route is promising and has many advantages, like being simple, cost-effective, fast, green synthesis, high purity product, and fair control of the core–shell dimensions [16–18].

2 Experimental

2.1 Preparation of Au@LiNbO$_3$ core–shell nanoparticles

Au nanoparticles colloidal were prepared by the pulsed laser ablation technique (PLAL). A high purity (99.9%) Au pellet was immersed in a vessel filled with 3 ml of distilled water and irradiated with the second harmonic beam (532 nm) of a Q-switched neodymium-doped yttrium aluminum garnet (Nd: YAG) laser with a pulse duration of 7 ns and a repetition frequency of 1 Hz, 70 laser pulses. Ablation of Au nanoparticles was carried out at a laser fluence of 1.5 J/cm^2. The experimental set up of the PLAL system is shown in Fig. 1. Z-cut LiNbO$_3$ wafer (purchased from BIOTAIN HONG KONG CO., LIMITED) with an area of 1 cm^2 was placed in the vessel filled with Au colloidal and then irradiated with 200 laser pulses at different laser fluences of (1.3, 1.6, 2, 2.2) J/cm^2, which are represented in the results as S$_1$, S$_2$, S$_3$ and S$_4$, respectively.

2.2 Characterization of Au@LiNbO$_3$ core–shell nanoparticles

UV–Vis spectrometer (Shimadzu UV-2550) used to measure optical absorption of colloidal Au nanoparticles, LN nanoparticles and Au@LiNbO$_3$ core–shell. X-ray diffraction (Panalytical X' Pert Pro) was employed to study the structural properties of Au@LiNbO$_3$ core–shell. Raman spectra were recorded using confocal Raman spectrometer (HORIBA XPLORA PLUS). Transmission electron microscopy (ZEISS LEO 912) was used to investigate the morphology and size of Au@LiNbO$_3$ core–shell.

2.3 Preparation of Au@LiNbO$_3$ core–shell/Si photodetector

To fabricate a hybrid Au@LiNbO$_3$/Silicon (Si) photodetector, a thin layer Au @ LiNbO$_3$ core–shell was deposited on p-type silicon to fabricate a heterojunction detector as shown in Fig. 2, the silicon has an electrical resistivity of 3–5 Ω cm and orientation of (111) by drop casting technique. These solutions were dropped by pipette on glass and Si substrate at 40 °C. The film thickness was measured using laser interferometer method. The electrical behavior in dark and under different illumination powers was measured.

3 Results and discussion

Figure 3 shows the optical absorption spectrum of Au nanoparticles and Au@LiNbO$_3$ core–shell synthesized at various laser fluences. Figure 3 shows a single absorption peak at 520 nm for Au nanoparticles, which is indexed to surface plasmon resonance (SPR) [19, 20]. The optical absorption plots of Au@ LiNbO$_3$ showed small absorption peaks located at 224, 215, 206, and 206 nm for samples S$_1$, S$_2$, S$_3$, and S$_4$, respectively, which belonged to the quantum
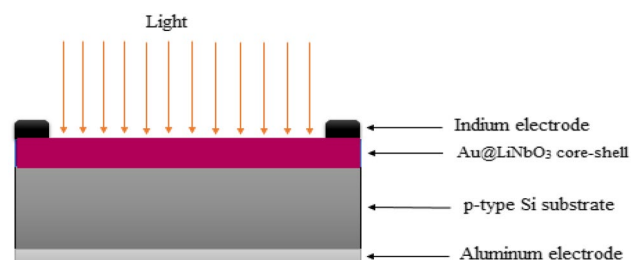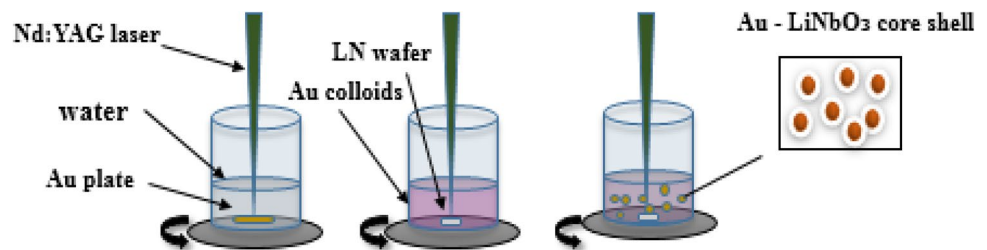
Fig. 2 Schematic diagram of Au@LiNbO$_3$/p-Si heterojunction

Fig. 1 Schematic diagram of detailed formation mechanism of Au @ LiNbO$_3$ core–shell nanoparticles by two-steps of laser ablation in water
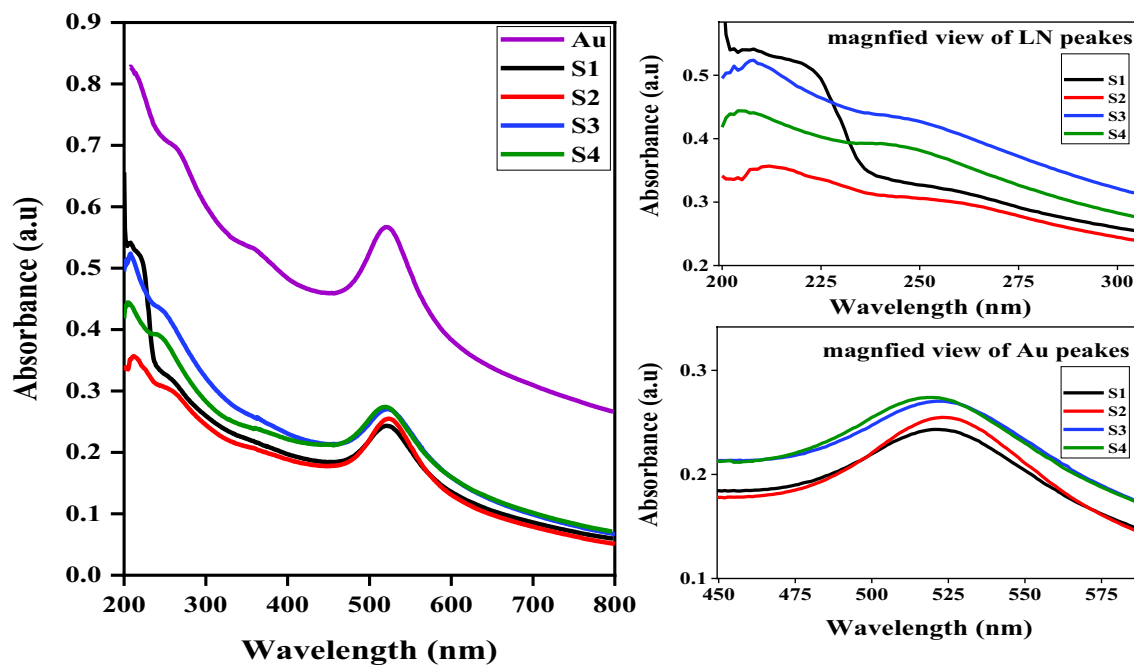
Fig. 3 UV–Vis spectra of the prepared Au@LiNbO₃ core -shell prepared at different laser fluences

size effect of LiNbO₃ nanoparticles. This absorption peaks value confirm by the 4 eV energy gap value indicate the absorption at UV region and reported by other [12]. Broad absorption peaks at 535, 533, 530, and 522 nm for S_1, S_2, S_3, and S_4, respectively, were detected, which belonged to Au nanoparticles at longer wavelength region as reported by other [19, 20]. The slight shift in absorption peaks (blue shift) of LiNbO₃ and Au with increasing laser fluence can be ascribed to the decrease in their particle size. The presence of both absorption peaks of LN and Au confirms the formation of Au@ LiNbO₃. From the absorption peak of Au, the particle size (d) of Au was estimated with the aid of the following equation [20]

$$d = e^{\frac{B_1 A_{prs}}{A_{450}} B_2} \qquad (1)$$

where B_1 and B_2 are constants equal to 3 and 2.2, respectively, and A_{prs} and A_{450} were the absorbance values at SPR and 450 nm, respectively. The UV–Vis spectrum of the colloidal Au solution (Fig. 3) shows an SPR peak at 520 nm and a 520/450 absorbance ratio equal to 1.23. After substituting the constants in Eq. 1, the particle was found to be 8 nm. The optical energy gap E_g of Au@LiNbO₃ core -shell was determined by extrapolating the linear part of $(\alpha h\nu)^2$ versus $(h\nu)$ plot to $(\alpha h\nu)^2 = 0$ point according to Tauc relation absorption coefficient (α) near the band edge for band to band and excitation transitions [21].

$$(\alpha h\nu)^2 = A^2 (h\nu - E_g)(2)$$

where α is the absorption coefficient and A is the constant. The optical energy gap of core–shell was 3.5, 3.6, 3.7, 3.8 eV for samples S_1, S_2, S_3, and S_4, respectively. The Increase in energy gap with increasing laser fluence is due to the reduction in particle size and this will produce a blue shift which will discuss later on. The energy gap of LiNbO₃ nanoparticles was around 5.5 eV and decreases after making core–shell with gold as shown in Fig. 4-a due to effect of SPR comes from Au (core) nanoparticles as shown in Fig. b. This result is consistent with reported data [12]. Figure 5 shows the x-ray diffraction patterns of the Au-LiNbO₃ core–shell prepared at various laser fluences. All samples are polycrystalline and the observed XRD peaks belonged to LiNbO₃ and Au, confirming the formation of an Au-LiNbO₃ core–shell structure. The sample prepared at 1.3 J/cm² exhibits seven peaks located at $2\theta = 33^0$, 44.5^0, 47^0, 54^0, 56^0, 57^0, 61^0, and 66.50, corresponding to (104), (200), (024), (116), (122), (118), (214), and (220), respectively.

The second and seventh peaks belong to face center cubic Au, while the other peaks are indexed to LiNbO₃ with a rhombohedral structure according to JCPDs#00-020-0631 [20]. The intensity and full width at half maximum of the XRD peaks were found to be increased after increasing the laser fluence > 1.6 J/cm² due to decreasing the particle size
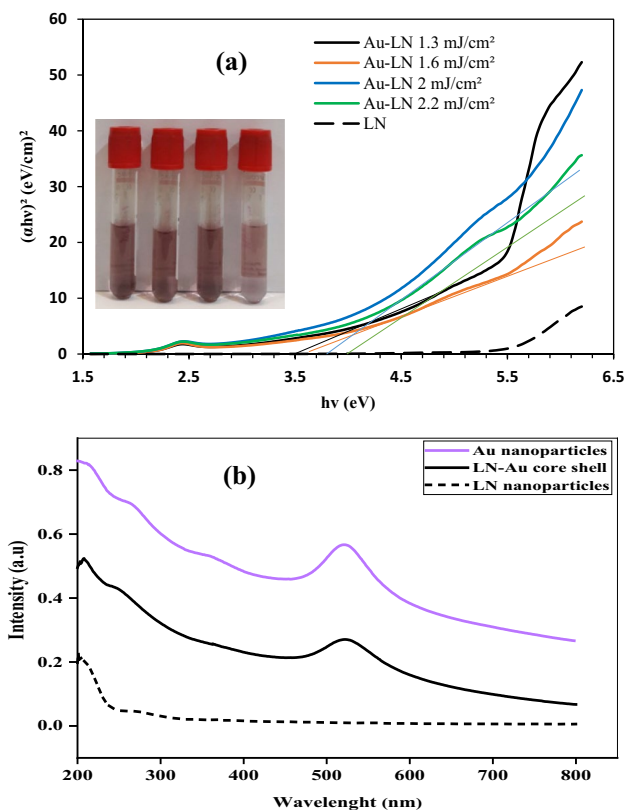
Fig. 4 $(\alpha h\nu)^2$ versus $h\nu$ plots of **a** Au@LiNbO$_3$ core–shell and **b** SPR in Au

of LiNbO$_3$ and increasing the concentration of particles. No peaks related to contamination or other phases were found, indicating the purity of the synthesized product.

The crystallite size of LiNbO$_3$ and Au@LiNbO$_3$ core–shell nanoparticles were determined from Scherrer equation as shown in Table 1. The crystallite size decreases as laser fluence increases. On the other hand, the dislocation density and strain of the synthesized nanoparticles were calculated as a function of laser fluence as revealed in Table 1.

The dislocation density and strain existed on the nanoparticles increased as laser fluence increased, since at higher laser fluence in the ablation process structural defects may occur as well as the quenching effect.

The Raman spectra of the Au@LiNbO$_3$ core–shell are presented in Fig. 6. As clearly seen, the samples prepared at 1.3–2.2 J/cm^2 has eight Raman vibration modes, namely, E-TO, 1A1TO, 3A1TO, E(LO6), E(LO7), A(TO4), A1 TO, and E(LO9). All these vibration modes are indexed to the z-cut LiNbO$_3$ single crystal [23]. The Raman peaks of core–shell samples are listed in Table 2, with their active modes. As indicated in Table 2, this result emphasizes that all observed phonon modes in Raman spectra for synthesized samples are in agreement with the reported modes for z-cut LiNbO$_3$ single crystal reported by other workers [22]. Peak appears at 526 cm^{-1} at 1.3–2.2 J/cm^2 laser energy. Because of a violation of the Raman selection constraints, these peaks are very certainly attributable to the two-phonon process [24, 25]. The obtained Raman bands have lower energy than bulk LN, as stated by other literature [26, 27], which is due to more relaxed binding in nanoparticles as the surface to volume ratio increases [17]. It is clear from Fig. 6 that a significant enhancement in the Raman intensity was observed for the LN@Au core–shell sample compared to that of LN nanoparticles due to the presence of plasmonic Au NPs, which play a vital role in the surface-enhanced Raman scattering. This can originate from the local fields associated with the excitation of surface plasmon resonances by the Raman source [23, 28, 29].

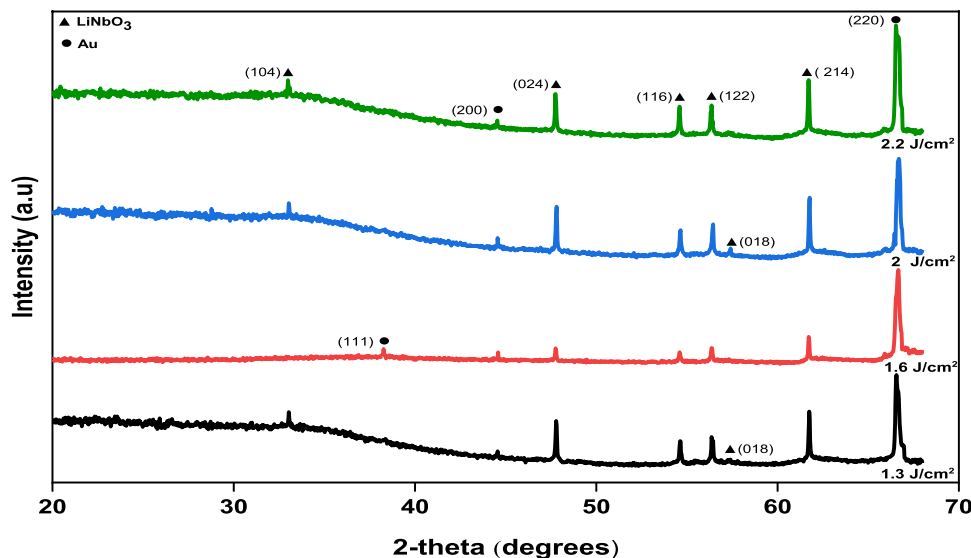**Fig. 5** XRD analysis of Au @ LN core–shell nanoparticles prepared at various laser fluences

Table 1 XRD parameters of Au @ LiNbO₃ core–shell prepared at various laser fluencies

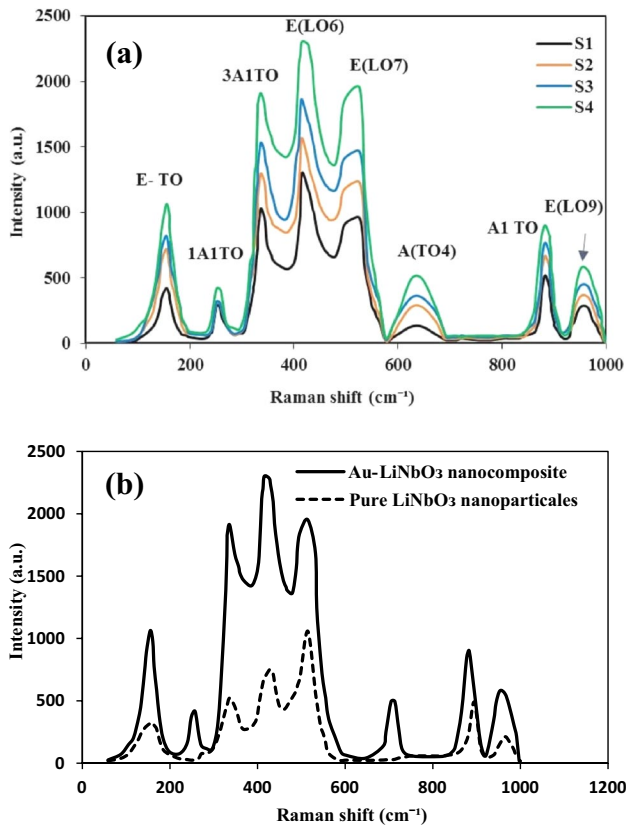| Laser fluence J/cm²	2- theta (degrees)	Orientation (hkl)	d – spacing (Å)	Grain size (nm)	Dislocation density (nm⁻²)	Strain
1.3	61.74946	214	1.748	69.3	3.6×10^{-5}	4×10^{-8}
1.6	61.72443	214	1.749	33.8	8.7×10^{-4}	7×10^{-8}
2	61.75788	214	1.748	27.5	1.3×10^{-3}	9×10^{-8}
2.2	61.73754	214	1.749	20.68	2.3×10^{-3}	1.2×10^{-7}

Fig. 6 Raman spectrum of **a** Au @ LN core–shell nanoparticles and **b** Raman spectra of Au @ LN and pure LN

Table 2 Raman peaks for LiNbO₃@Au core shell prepared at different laser energy

Modes	Reported	Measured			
		1.3 J/cm²	1.6 J/cm²	2 J/cm²	2.2 J/cm²
E-TO	152 [28]	154	154	154	154
1A1TO	252 [28]	251	251	251	251
3A1TO	334 [28]	336	336	336	336
E(LO6)	424 [27]	415	415	415	415
E(LO7)	524 [27]	526	526	526	526
A(TO4)	625 [27]	625	625	625	625
A1 TO	883 [22, 30]	883	883	883	883
E(LO9)	988 [27]	953	953	953	953

Table 2 shows the vibration modes of LN and Au @ LN core–shell nanoparticles prepared at various laser fluences compared to those reported in the literature.

As shown in Fig. 7, the morphology and size of nanoparticles are found to be greatly dependent on the laser fluence. The nanoparticles prepared at a laser fluence of 1.3 J/cm² exhibited spherical nanoparticles with an average particle size of 78 nm. The average core size was 65 nm and the average shell thickness was 13 nm. The average particle size decreased to 31 nm after increasing the laser fluence to 1.6 J/cm². Further increases in the laser fluence lead to a decrease in the particle size of 22 nm. The decreasing particle size with laser fluence can be attributed to the characteristics of the produced plasma plum on the target's surface as a result of the interaction of a high power laser pulse with a solid target and then with the plasma species itself. With increased laser pulse energy, larger nanoparticles could easily be broken into tiny fractions upon interaction with intense laser pulses. Throughout this case, the number density of smaller particles rises at the expense of larger particle density, which is in agreement with the increase in the absorption in the UV [31, 32]. From TEM images with the help of image J software, the particle size distribution (PSD) of the samples prepared at different laser fluences is shown in Fig. 7.

Figure 8 shows the variation of both core size and shell thickness with the laser fluence. The core size decreases from 65 to 20 nm and the shell thickness decreases from 13 to 5 nm as laser fluence increases from 1.3 to 2.2 J/cm². As shown in Fig. 8, the irradiation of the sample at a laser fluence of 2.2 J/cm² results in the formation of a shell with a thickness larger than the core size. This result can be attributed to the mismatch in the lattice constants of LiNbO₃ and Au nanoparticles, which in turn induced compressive stress and squeezed the core and increased the shell thickness [33]. Figure 9 shows the variation of core diameter and shell thickness with laser fluence. With increasing laser fluence, core diameter and shell thickness both decrease. Also, it is noticed that the Au core diameter is larger than the LN shell thickness for different laser fluences.

Field Emission Scanning Electron Microscope (FESEM) of Au @ LN thin films prepared at a different laser fluence of 1.6–2.2 J/cm² was examined as shown in Fig. 10. The surface morphology of Au@LN core–shell shows the particle
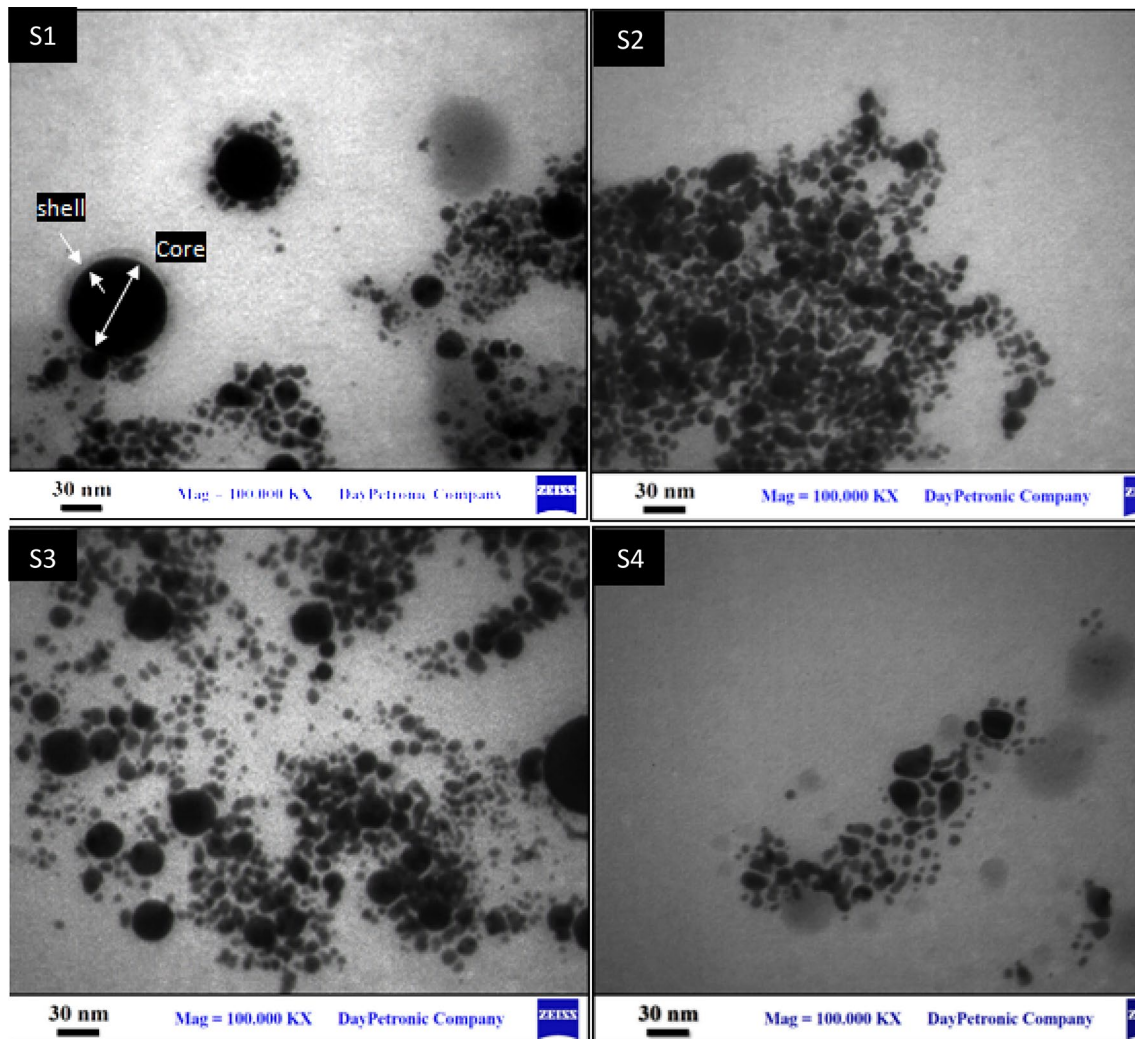
Fig. 7 Transmission electron microscopy of Au @ LN nanoparticles at different laser fluence (S_1) 1.3 J/cm^2, (S_2) 1.6 J/cm^2, (S_3) 2 J/cm^2, and (S_4) 2.2 J/cm^2

size decreased as laser fluence increased. The deposited films exhibit gradually a uniform and dense surface with merged particles' boundaries. Also, it showed a decrease in particles aggregation as laser fluence increased.

Hall measurements were conducted and they find that all Au@LiNbO$_3$ films have positive Hall coefficient indicates these films are p-type. Figure 11 shows variation of Hall mobility of and hole (h) concentration of Au@LiNbO$_3$ film with laser fluence. The mobility of the films increased as laser fluence increases due to the low concentration of grain boundaries as well as decreasing in the particles agglomeration. The carrier concentration increases slightly in the beginning as laser fluence increases and then sharply increased at laser fluence of 2.2 J/cm^2.

For detector performance investigations it is important to know the films thicknesses and particle density, both were estimated and found to be about 101, 113, 123, and 99 nm,

while the particle density are 1.34×1012, 1.33×1013, 1.32×1013, and 1.32×1017 particles/cm3 for films prepared with different laser fluences 1.3, 1.6, 2, and 2.2 J/cm^2, respectively.

Figure 12 shows the current–voltage (I–V) characteristics of the p-Au@LiNbO$_3$/p-Si heterojunction (HJs) prepared at different laser fluences in dark conditions. At the forward bias, the current increases slightly with the bias voltage and then exponentially with the voltage after 3 V. In the first region, the recombination current is larger than the generation current, and the diffusion current dominates in the second region [34, 35]. For bias voltages greater than 3 V, the carriers have energy greater than the barrier height of the junction and conduct the current. Figure 11 confirms that the heterojunctions exhibit rectification behavior with a rectification factor depending on the laser fluence. The sample prepared at a laser fluence of 2.2 J/cm^2 has the maximum
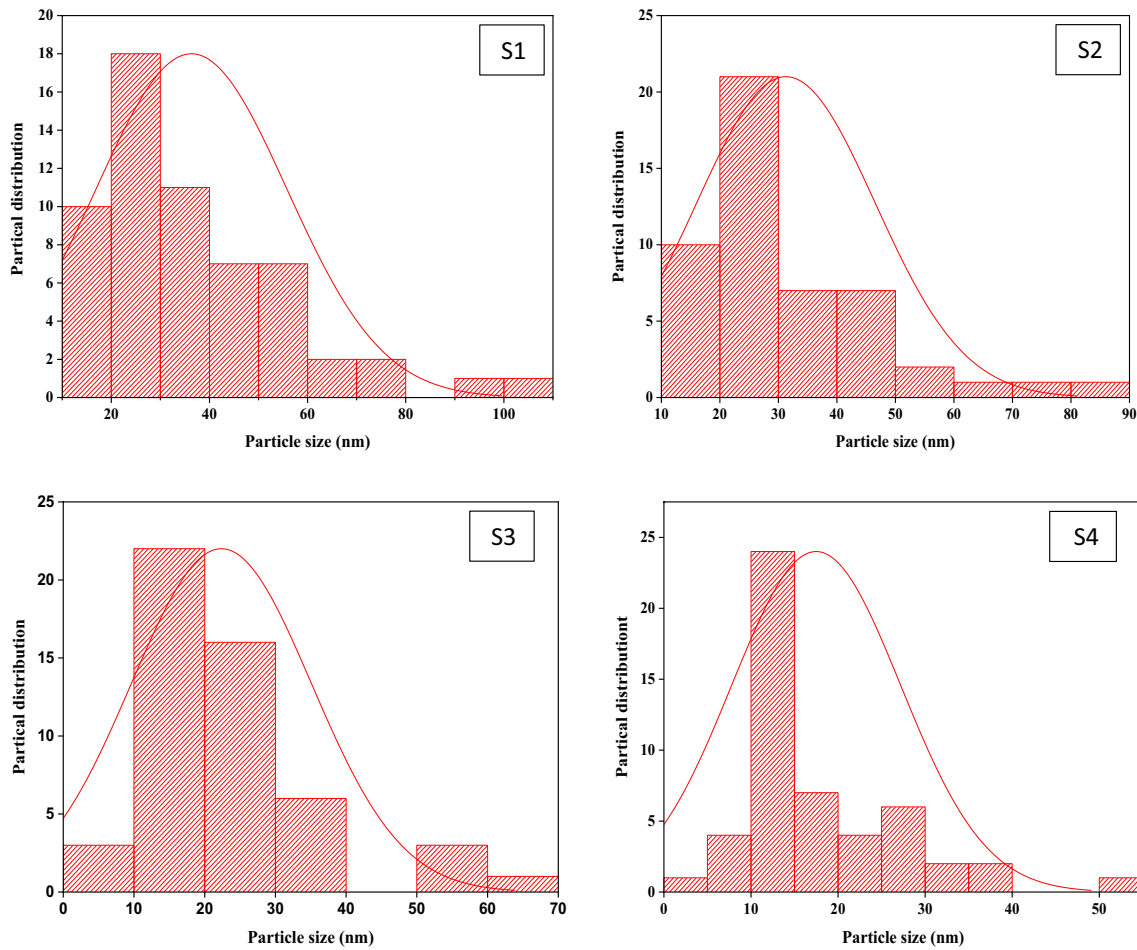
Fig. 8 Histogram distribution of TEM results of Au @ LN nanoparticles at different laser fluence of (S$_1$) 1.3 J/cm^2, (S$_2$) 1.6 J/cm^2, (S$_3$) 2 J/cm^2, and (S$_4$) 2.2 J/cm^2
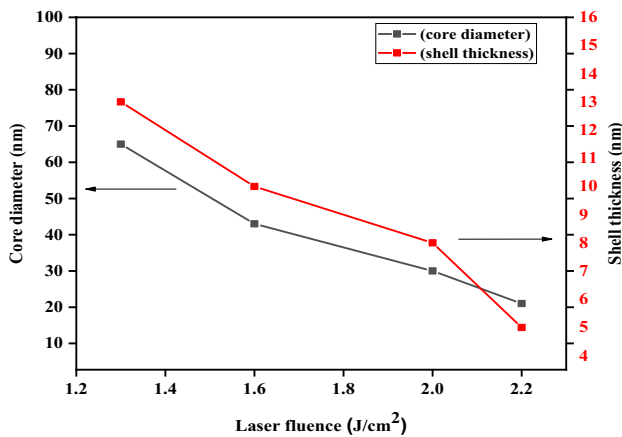

Fig. 9 Core diameter and shell thickness of Au @ LN nanoparticles as a function of laser fluence

forward current. This could be attributed to the large surface area and low electrical resistivity of LN layer that arise from the reduction in structural defects. The leakage current of the heterojunctions increases slightly with bias voltage after −4 V. The ideality factor of the heterojunction was determined from the diode equation. The ideality factors for the heterojunctions fabricated at laser fluence of 1.3, 1.6, 2, and 2.2 J/cm^2 were 4.3, 4.1, 3, and 2.5, respectively. The large value of the ideality factor indicates the presence of surface states and trapping centers at the Au@LiNbO₃-Si interface [36, 37] as well as due to a mismatch in lattice constants of Au@LiNbO₃ and the Si substrate.

The illuminated current–voltage characteristics of the Au@LiNbO₃/p-Si HJ photodetectors at reverse bias under white illumination at various light intensities (3.2, 7.7, 15.1, and 28.3) mW/cm^2 are shown in Fig. 13.

The photocurrent increased after illumination as a result of the formation of electron–hole (e–h) pairs at the depletion layer where the electric field prevents e–h recombination. The maximum current was found for the
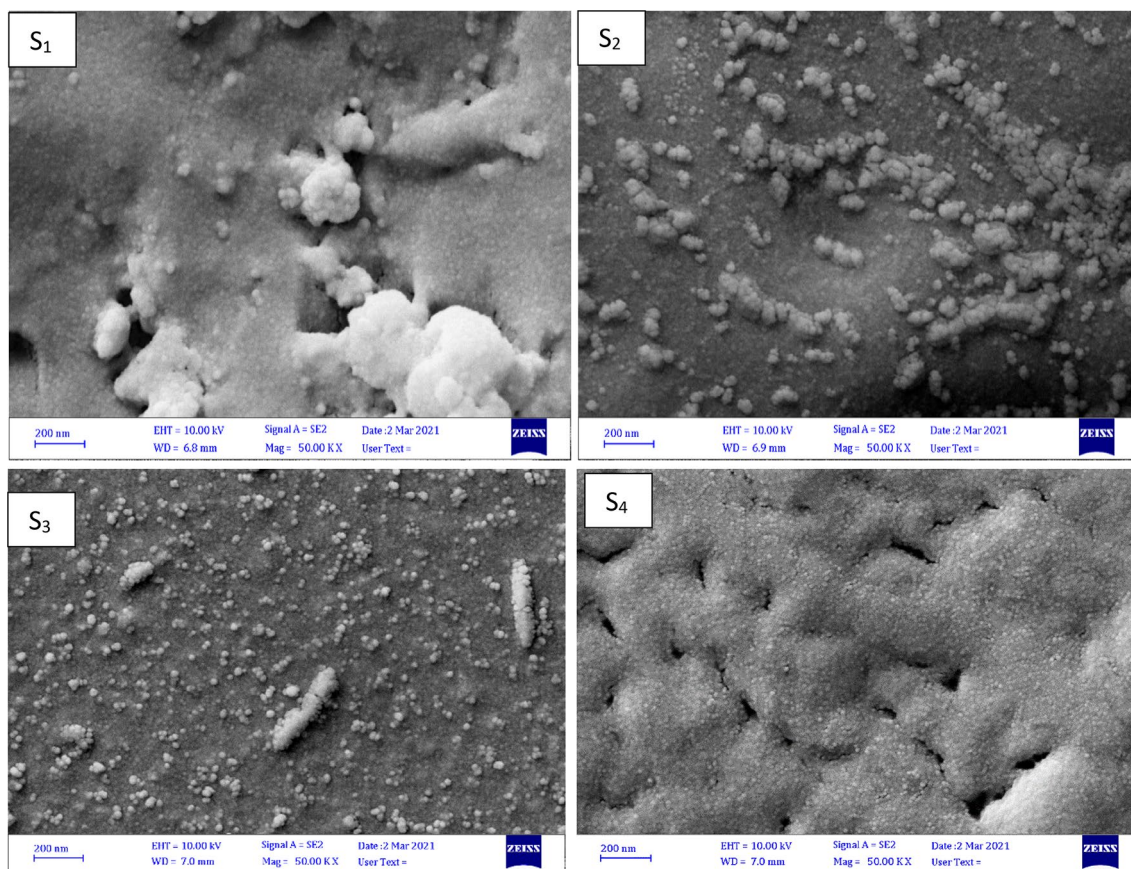
Fig. 10 Field Emission Scanning Electron Microscope (FESEM) of Au @ LN nanoparticles at different laser fluence (S_1) 1.3 J/cm^2, (S_2) 1.6 J/cm^2, (S_3) 2 J/cm^2, and (S_4) 2.2 J/cm^2
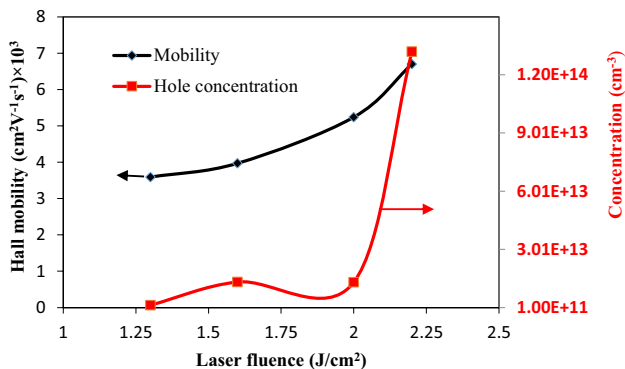

Fig. 11 Hall mobility and hole concentration of Au@LiNbO$_3$ as a function of laser fluence
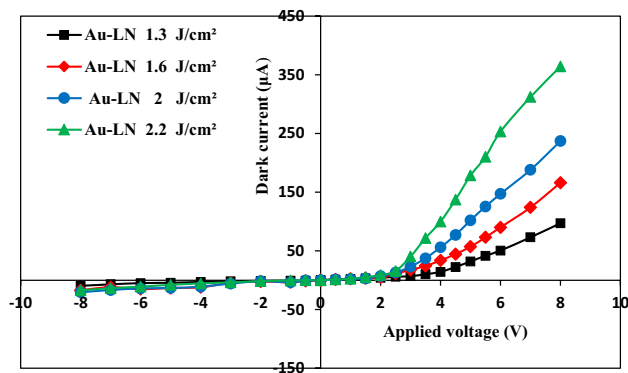

Fig. 12 Dark I-V characteristic of p-Au @ LiNbO$_3$/p-Si heterojunction under forward and reverse bias prepared at different laser fluences

photodetector prepared at 2.2 J/cm^2. This could be correlated to the structural and optical properties of the Au @ LN core–shell. On the other hand, the photocurrent is increased after increasing the light intensity due to the increasing number of generated e–h pairs that come from increasing the absorbed photons, which indicates the

photodetectors have good linearity characteristics. The external bias also contributes significantly to increasing the photocurrent via widening the depletion region and plays a vital role in decreasing the carrier's recombination process. The ON/OFF ratio of the photodetector at 8 V
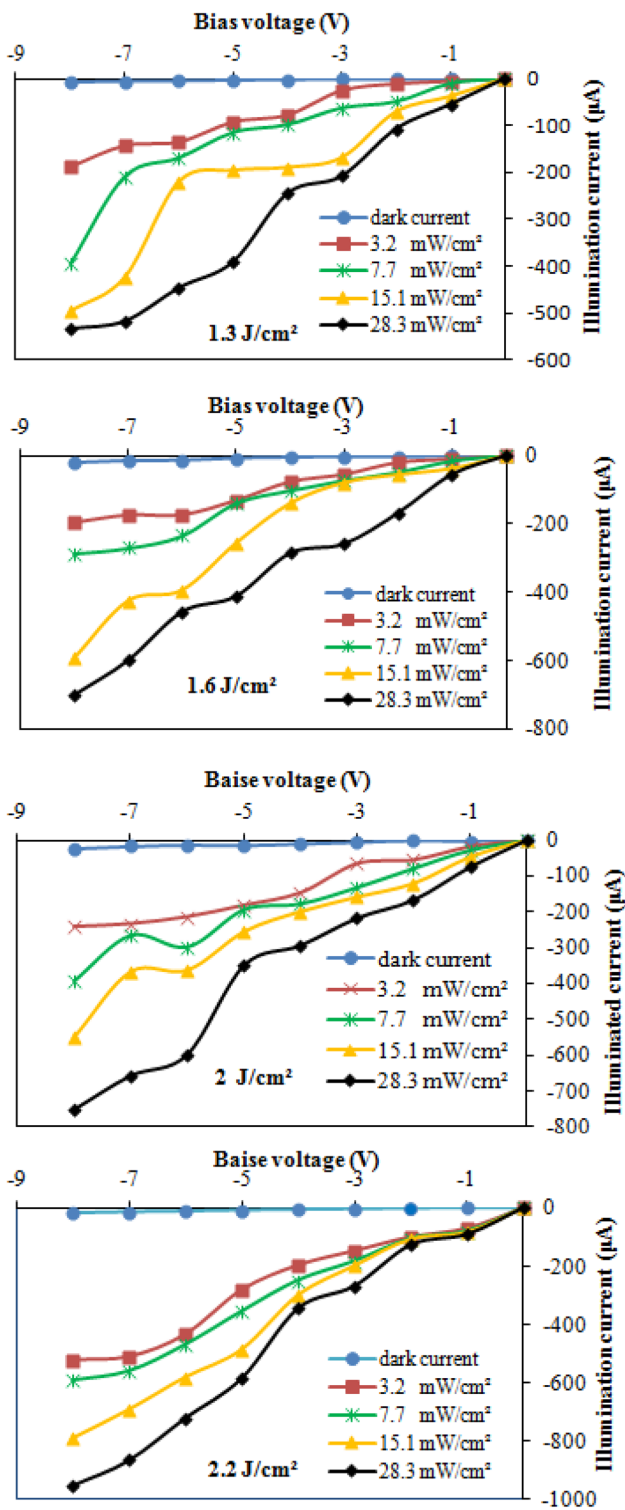
Fig. 13 Dark and illuminated (I–V) characteristics of Au@LiNbO₃/p-Si HJs photodetectors prepared at different laser fluences
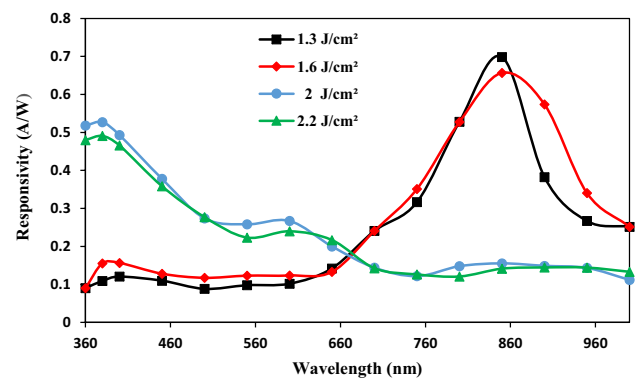

Fig. 14 Spectral responsivity of Au @ LiNbO₃/p-Si HJs photodetectors prepared at different laser fluences

due to an increase in the surface area and high concentration of Au@LN core–shell nanoparticles. Figure 14 presents the spectral responsivity of the Au@LN/p-Si heterojunction photodetector at a reverse bias voltage of 5 V. It has detected that devices prepared at low laser fluence of 1.3 and 1.6 J/cm^2 exhibited two peaks of response. The first small peak was observed at 380 nm due to the absorption edge of the LN film, and the second peak was found at 850, which may be related to light absorbed in the depletion region of the silicon substrate [38, 39]. The maximum responsivity was 0.69 A/W at 380 nm and 0.65 A/W at 850 nm for the photodetector prepared at 1.3 J/cm^2. The dependence of the responsivity of the photodetector on laser fluence may be attributed to the shell thickness increasing as the laser fluence increased, which in turn decreased the amount of light that penetrates the Au core. On the other hand, the SPR of Au enhanced the responsivity at 500 nm. The specific detectivity (D*) and external quantum efficiency (EQE) of the photodetectors were determined as a function of laser fluence as shown in Table 3. The maximum value of EQE was 1.7×10^2% at 380 nm for a photodetector prepared at 2 J/cm^2. This

Table 3 Figures of merit of the fabricated Au @ LiNbO₃/Si HJs photodetectors

Laser fluence J/cm^2	Wavelength (nm)	Detectivity $\times 10^{12}$ (Jones)	NEP (pW)	EQE (%)
1.3	400	1.1	0.9	37
	850	6.5	0.15	101
1.6	400	1.5	0.66	50
	850	6.5	0.15	95
2	380	5.5	0.18	172
	850	1.6	0.62	22
2.2	380	5.1	0.19	166
	850	1.4	0.71	20

bias and light intensity of 28.3 mW/cm^2 increased from 90 to 136 after increasing the laser fluence from 1.3 to 2.2 J/cm^2. The increase in ON/OFF ratio with laser fluence is
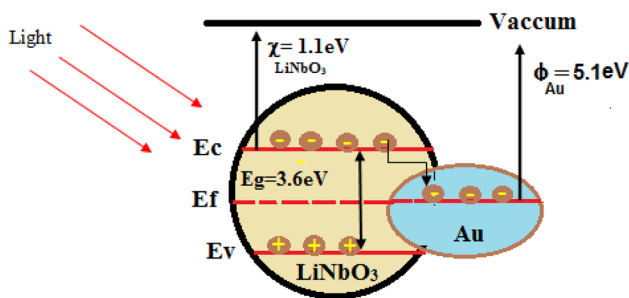
Fig. 15 Energy band diagram of Au @ LiNbO$_3$ core–shell under illumination

result is due to the high absorption of light at the LN shell and produces a large number of e–h pairs. This indicates the high value of carrier collection efficiency. The maximum D^* of Au@LN/ p-Si photodetector was 5.5×10^{12} and 6.5×10^{12} Jones at 380 nm and 850 nm, respectively. The presence of Au nanoparticles plays an essential role in preventing the e–h recombination due to the high electric field region and via the substituting of LN with electrons and increasing the photocurrent [40, 41].

Table 3 presents the effect of different laser fluence on specific detectivity, noise equivalent power, and quantum efficiency for Au @ LN /Si HJs photodetectors. Results show effect of laser fluence on the specific detectivity of for Au @ LN /Si photodetector as shown, the highest value of D^* for 1.3 and 1.6 J/cm^2 laser fluence is at 850 nm wavelength, while at higher laser fluence of 2 and 2.2 J/cm^2 is at 380 nm laser fluence. The high value of D^* for the photodetector prepared at 2 and 2.2 J/cm^2 laser fluence indicates this photodetector can be used for small signal detection applications. The maximum value of EQE (1.7×10^2% at 380 nm) indicates that this photodetector prepared at 2 J/cm^2 has minimum recombination losses and high collection efficiency of the generated carriers. The responsivity in the visible for the Au@LiNbO$_3$/Si photodetector fabricated at 2 J/cm^2 is higher than that of other heterojunction-based silicon photodetectors.

The energy band diagram of the Au@LiNbO$_3$ core–shell under illumination is shown in Fig. 15. As clearly shown, when the light is incident on the LiNbO$_3$ side, it will produce an e–h pair. Because the work function (Φ) of Au about 5.1 eV is greater than that of LiNbO$_3$, the electrons transfer from the conduction band of LN to Au, increasing the photocurrent. This indicates that the presence of an Au core plays a vital role in increasing the responsivity of the LiNbO$_3$/Si photodetector via a reduction in the recombination of e–h pair. The band offsets ΔEc and ΔEv between LiNbO$_3$ and p-Si were determined and found to be 2.95 eV and 0.47 eV, respectively. The ΔEc is large and the electron transfer from Si to LN and therefore the presence of Au will contribute in electron transfer when illuminated with light.

4 Conclusion

Au@LiNbO$_3$ core–shell nanoparticles were successfully synthesized using two steps of laser ablation in liquid. The particle size was decreased, depending on the laser fluence. The shell thickness increased with laser fluence. The XRD results revealed that all the samples are crystalline with rhombohedral LiNbO$_3$ and center cubic Au. The particle size also decreased, as TEM demonstrated. The optical energy gap of LiNbO$_3$ decreased after making Au@LiNbO$_3$. The optical energy gap is 4.8 eV for LiNbO$_3$ nanoparticles, while it decreases to 3.8 eV for Au@LiNbO$_3$ core–shell nanoparticles. The energy gap of core–shell nanoparticles increases as the laser fluence increases. When compared to LiNbO$_3$, the Raman results show a significantly enhanced surface plasmon resonance of the core–shell. The main figures of merit of the photodetectors, namely, responsivity, specific detectivity, noise equivalent power, and external quantum efficiency of the photodetector were studied as a function of laser fluence. The results of the photodetectors are correlated with the optical, structural and electrical properties of Au@LiNbO$_3$ nanostructure. A UV-enhanced maximum responsivity of 0.69A/W at 380 nm and 0.65A/W at 850 nm was found for Au@LiNbO$_3$/Si photodetector fabricated at laser fluence of 2 J/cm^2.

Author contributions RAI and ETS conceived of the presented idea. RAI and ETS supervised the finding of this work. MSA conducted the experiments. All authors discussed the results and contributed equally to the final manuscript. All authors provided critical feedback and helped shape the research, analysis and manuscript.

Availability of data and materials Not applicable.

Declarations

Conflict of interest The authors have declared no conflict of interest.

Ethics approval Not applicable.

Consent to participate Not applicable.

Consent for publication Not applicable.

References

1. Y. Zhao, S. Li, Y. Zeng, Y. Jiang, APL Mater. **3**, 8 (2015)
2. S. Thatai, P. Khurana, J. Boken, S. Prasad, D. Kumar, Microchem. J. **116**, 62–76 (2014)
3. D. Sun, G. Zhang, J. Huang, H. Wang, Q. Li, Mater (Basel) **7**(2), 1360–1369 (2014)
4. M.B. Gawande et al., Chem. Soc. Rev. **44**(21), 7540–7590 (2015)
5. P. Khurana et al., Plasmonics **8**, 2 (2013)
6. S.V. Salihov et al., J. Magn. Magn. Mater. **394**, 173–178 (2015)
7. J. Richter et al., Nanoscale **6**, 10 (2014)
8. S.P. Pogossian, H. Le Gall, J. Appl. Phys. **93**, 5 (2003)
9. T.C. Lee, J.T. Lee, M.A. Robert, S. Wang, T.A. Rabson, Appl. Phys. Lett. **82**, 2 (2003)
10. R.F. Ali, M. Bilton, B.D. Gates, Nanoscale Adv. **1**, 6 (2019)
11. C. Debnath, S. Kar, S. Verma, K. S. Bartwal **15**, 5 (2015)
12. A. Tumuluri, K. Lakshun Naidu, K.C. James Raju, Int. J. Chem. Tech. Res. **6**, 6 (2014)
13. B. Ghosh, D. Chakravorty, G.C. Das, J. Appl. Phys. **100**, 9 (2006)
14. L. Haoa, Y. Lib, J. Zhu, Z. Wu, J. Deng, AIP Adv. **3**, 042106 (2013)
15. W. Li, J. Cui, D. Zheng, Basel **12**, 2659 (2019)
16. W.T. Nichols, T. Sasaki, N. Koshizaki, J. Appl. Phys. **100**, 11 (2006)
17. M.H.A. Raid, A. Ismail, A.M. Mousa, Mater. Res. Express **29**, 27 (2018)
18. R.S.A.H. Raid, A. Ismail, Mater. Res. Express **4**, 125020 (2017)
19. E. Greco et al., J. Nanoparticle Res. **22**, 6 (2020)
20. W. Haiss, Anal. Chem, 34, (2008).
21. K.A. Aadim, A.Z. Mohammad, M.A. Abduljabbar, I.O.P. Conf, Ser. Mater. Sci. Eng. **454**, 1 (2018)
22. D. Mohanty, G.S. Chaubey, A. Yourdkhani, S. Adireddy, G. Caruntu, J.B. Wiley, RSC Adv. **2**, 5 (2012)
23. A.C. Santulli, H. Zhou, S. Berweger, M.B. Raschke, E. Sutter, S.S. Wong **12**, 10 (2010)
24. F. Meriche et al., Opt. Mater. (Amst) **32**, 11 (2010)
25. R.F. Ali, B.D. Gates, Chem. Mater. **30**, 6 (2018)
26. X.N. He et al., Nanotechnology **23**, 20 (2012)
27. M.A. Fakhri, E.T. Salim, M.H.A. Wahid, A.W. Abdulwahhab, Z.T. Salim, U. Hashim, J. Phys. Chem. Solids **131**, 180–188 (2019)
28. Y. Kobayashi et al., J. Phys. J. Phys. Conf. Ser. **918**, 012035 (2017)
29. M.A. Fakhri, Y. Al-Douri, U. Hashim, E.T. Salim, Sol. Energy **120**, 381–388 (2015)
30. S. Shandilya, A. Sharma, M. Tomar, V. Gupta, Thin Solid Films **520**, 6 (2012)
31. N. Mirghassemzadeh, M. Ghamkhari, D. Dorranian, Soft Nanosci. Lett. **03**(04), 101–106 (2013)
32. D. Dorranian, E. Solati, L. Dejam, Appl. Phys. A Mater. Sci. Process. **109**, 2 (2012)
33. N. Gheshlaghi, M. Faraji, H. Sedaghat Pisheh, Appl. Sci. **2**, 4 (2020)
34. R. Ismail, K. Hassan, O. Abdulrazaq, W. Abode, Mater. Sci. Semicond. Process **10**, 19–23 (2007)
35. E. Salim, R. Ismail, M. Fakhri,B. Rasheed, Z. Salim Iran J. Sci. Technol. Trans. Sci., 43 (2019)
36. R. Ismail, S, Zaidan, R. Kadhim Appl. Nanosci., 7, (2017)
37. R. Ismail, R. Abdul-Hamed, Mate. Res. Exp. **4**, 12050 (2017)
38. A.M. Mousa, R.A. Ismail, M.H. Amin, Opt. Int. J. Light Electron Opt. **183**, 933–941 (2019)
39. S. Gunasekaran, D. Thangaraju, R. Marnadu et al., Sens. Actuators A: Phys. **317**, 112373 (2021)
40. R.A. Ismail, K.S. Khashan, M.F. Jawad, A.M. Mousa, F. Mahdi, Mater. Res. Express **5**, 55018 (2018)
41. R.A. Ismail, J Semiconductor Technol. Sci. **9**, 51–54 (2009)